Monthly Notices of the ROYAL ASTRONOMICAL SOCIETY

MNRAS **502,** 510–520 (2021) doi:10.1093/mnras/staa3829
Advance Access publication 2020 December 16

Spectroscopy of the first resolved strongly lensed Type Ia supernova iPTF16geu

J. Johansson,[1,2]★ A. Goobar,[2] S. H. Price,[3] A. Sagués Carracedo,[2] L. Della Bruna,[4] P. E. Nugent,[5,6] S. Dhawan,[2] E. Mörtsell,[2] S. Papadogiannakis,[2] R. Amanullah,[2] D. Goldstein,[7] S. B. Cenko,[8,9] K. De,[7] A. Dugas,[7] M. M. Kasliwal,[7] S. R. Kulkarni[7] and R. Lunnan[4]

[1]*Department of Physics and Astronomy, Division of Astronomy and Space Physics, Uppsala University, Box 516, SE-751 20 Uppsala, Sweden*
[2]*The Oskar Klein Centre, Physics Department, Stockholm University, Albanova University Center, SE-106 91 Stockholm, Sweden*
[3]*Max-Planck-Institut für Extraterrestrische Physik, Postfach 1312, D-85741 Garching, Germany*
[4]*The Oskar Klein Centre, Department of Astronomy, Stockholm University, AlbaNova University Centre, SE-106 91 Stockholm, Sweden*
[5]*Lawrence Berkeley National Laboratory, 1 Cyclotron Road, Berkeley, CA 94720, USA*
[6]*Department of Astronomy, University of California, Berkeley, CA 94720, USA*
[7]*Division of Physics, Mathematics and Astronomy, California Institute of Technology, Pasadena, CA 91125, USA*
[8]*Astrophysics Science Division, NASA Goddard Space Flight Center, MC 661, Greenbelt, MD 20771, USA*
[9]*Joint Space-Science Institute, University of Maryland, College Park, MD 20742, USA*

Accepted 2020 December 8. Received 2020 November 24; in original form 2020 April 23

ABSTRACT

We report the results from spectroscopic observations of the multiple images of the strongly lensed Type Ia supernova (SN Ia), iPTF16geu, obtained with ground-based telescopes and the *Hubble Space Telescope (HST)*. From a single epoch of slitless spectroscopy with *HST*, we resolve spectra of individual lensed supernova images for the first time. This allows us to perform an independent measurement of the time-delay between the two brightest images, $\Delta t = 1.4 \pm 5.0$ d, which is consistent with the time-delay measured from the light curves. We also present measurements of narrow emission and absorption lines characterizing the interstellar medium in the SN Ia host galaxy at $z = 0.4087$, as well as in the foreground lensing galaxy at $z = 0.2163$. We detect strong Na ID absorption in the host galaxy, indicating that iPTF16geu belongs to a subclass of SNe Ia displaying 'anomalously' large Na ID column densities compared to dust extinction derived from light curves. For the lens galaxy, we refine the measurement of the velocity dispersion, $\sigma = 129 \pm 4$ km s^{-1}, which significantly constrains the lens model. We use ground-based spectroscopy, boosted by a factor ∼70 from lensing magnification, to study the properties of a high-z SN Ia with unprecedented signal-to-noise ratio. The spectral properties of the supernova, such as pseudo-Equivalent widths of several absorption features and velocities of the Si II-line, indicate that iPTF16geu is a normal SN Ia. We do not detect any significant deviations of the SN spectral energy distribution from microlensing of the SN photosphere by stars and compact objects in the lensing galaxy.

Key words: gravitational lensing: strong – supernovae: general – supernova: individual (iPTF16geu).

1 INTRODUCTION

More than half a century has passed since Refsdal (1964) proposed to measure the expansion rate of the Universe, the Hubble parameter, using time delay measurements of multiply imaged gravitationally lensed supernovae (SNe). Thanks to the new generation of large time domain surveys, we are entering a phase where we can expect this technique to flourish (Goobar et al. 2002; Oguri & Marshall 2010; Goldstein & Nugent 2017; Goldstein, Nugent & Goobar 2019; Huber et al. 2019; Suyu et al. 2020). We refer to Oguri (2019) for an excellent review of the field of lensing of explosive transients.

The first case of a spatially resolved SN Ia is iPTF16geu (Goobar et al. 2017), a four-image gravitational lens system, and the subject of this work. In accompanying papers (Dhawan et al. 2020; Mörtsell et al. 2020), we report on the photometric measurements of time-delays, extinction, and magnification of iPTF16geu as well as the lens model. In addition to the time-delay estimates from photometric measurements, the well-known temporal spectral evolution of SNe Ia (Hsiao et al. 2007) can also be used to constrain the time-delay between images, through spatially resolved spectroscopy. We have obtained *HST* data for this purpose.

The high lensing amplification, $\mu \sim 70$, allows us to obtain very high signal-to-noise ratio spectroscopic observations that can be used to test the 'standard candle' nature of SNe Ia, as done previously for PS1-10afx by Petrushevska et al. (2017). Furthermore, the amplification allows for spectroscopy with high spectral resolution, otherwise unfeasible for high-redshift SNe. These observations allow us also to scrutinize the host and lens galaxy properties.

The large difference in the relative magnification between the four SN images, in spite of the spatial symmetry, suggests that micro-lensing by compact objects or milli-lensing by dark matter substructures in the lensing galaxy is significant (see e.g. More et al. 2017; Yahalomi, Schechter & Wambsganss 2017; Foxley-Marrable et al. 2018; Mörtsell et al. 2020). The impact of microlensing of strongly lensed SNe has been quantified by Dobler & Keeton (2006)

★ E-mail: joeljo@fysik.su.se

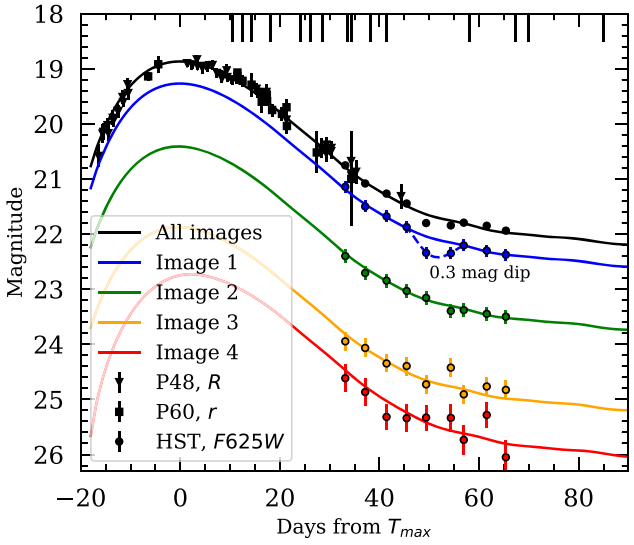

Figure 1. Black symbols and line show the *HST F*625*W* and ground-based *R*/*r*-band photometry and light-curve fit of iPTF16geu (all four images summed, *s*-corrected to *r* band). The blue, green, yellow and red symbols and lines show the resolved *HST F*625*W* photometry and light-curve fits for Images 1, 2, 3 and 4, respectively. We note a small dip (∼0.3 mag) in the light curve of Image 1, not seen for the other SN images nor in the *F*475*W* and *F*814*W* data. Vertical black lines indicate when the spectra were observed.

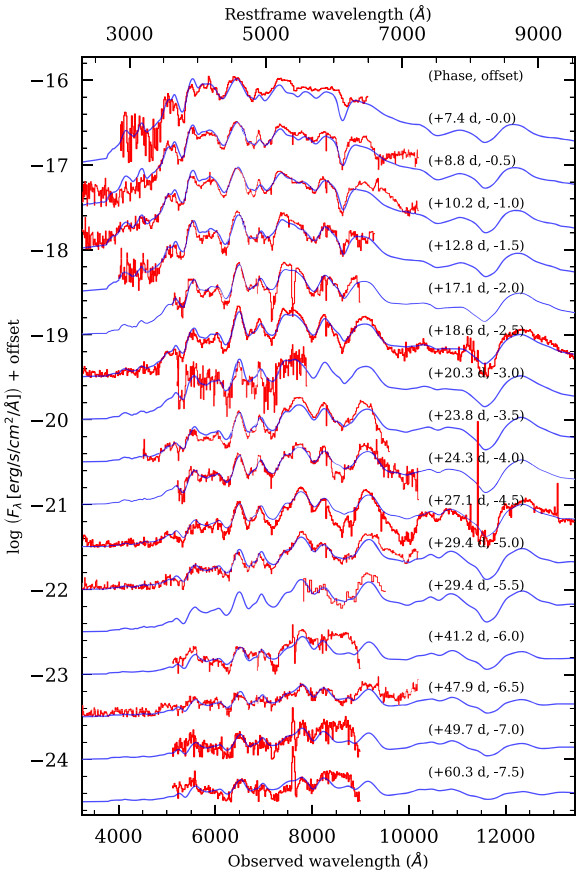

Figure 2. Time series of all spectra of iPTF16geu. The spectra (red lines) have been corrected for lens and host galaxy contamination. Blue lines are reddened Hsiao template SEDs at the same epochs.

and, more recently, Goldstein et al. (2018), Huber et al. (2019), and Pierel & Rodney (2019) carried out simulations including the effect of an expanding SN photosphere to show that microlensing often induces chromatic effects on the supernova spectrum, most noticeable starting about a month after the explosion. Here, we explore this possibility using a time series of iPTF16geu spectra.

The paper is organized as follows: First, in Section 2, we describe the photometric and spectroscopic data that we will use in our analysis. Then, in Section 3, we construct a model spectral energy distribution (SED) of the lens and host galaxy, that we can subtract from our observed spectra. We also analyse emission and absorption lines in our highest resolution spectra, probing the velocity dispersion of the lens and the interstellar medium of the host galaxy of iPTF16geu. In Section 4, we analyse the time-evolution of the SN features, measuring their pseudo-equivalent widths and expansion velocities. In Section 5, we analyse our single epoch of slitless spectroscopy with *HST*, and perform an independent measurement of the time-delay between the brightest SN images. We conclude with a discussion, summary, and future outlook in Sections 6 and 7.

2 OBSERVATIONS

The main focus of this paper is the analysis of the ground- and space-based spectroscopic observations of iPTF16geu. In order to accurately account for the lens and host galaxy contribution to the observed SN spectra we will use the *HST* and ground-based photometry described in Goobar et al. (2017) and Dhawan et al. (2020).

Figs 1, 2, and 3 illustrate the observations used in this work. Fig. 1 shows the ground-based Palomar 48- and 60-inch telescopes, P48 *R* and P60 *r* band and *HST F*625*W* light curves of the four SN images (summed light curves in black, and spatially resolved photometry for Images 1, 2, 3, and 4 in blue, green, orange, and red, respectively. The positions and labelling of the SN images are shown in Fig. 3).

The epochs of spectroscopic observations are indicated by black, vertical lines.

2.1 Photometry

Dhawan et al. (2020) present *HST* photometry of the four resolved SN images, and fit the individual light curves together with the summed photometry from ground-based telescopes. For Image 1 (the brightest image, see Fig. 3), they find $T_{\rm max,\,1} = 57\,652.80 \pm 0.33$ (MJD, which we will refer to as the time of maximum light) and a stretch $s = 0.99 \pm 0.01$. The measured time delays between the four images are consistent with being less than 1 d and the four lines of sight through the host and lensing galaxy experience differential extinction. Furthermore, the lensing analyses in More et al. (2017) and Mörtsell et al. (2020) indicate that iPTF16geu, especially the brightest image (Image 1), is likely affected by additional 'micro-lensing' from sub-structures in the lens galaxy halo.

We make use of the resolved *HST* and ground-based SN photometry presented in Goobar et al. (2017) and Dhawan et al. (2020). In Section 3, we also use of pre- and post-SN photometry of the lens and host galaxy system from the SDSS, PS1 and 2MASS surveys as well as the *HST* reference images.

2.2 Spectroscopy

A summary of our spectroscopic observations are listed in Table 1 and the time series of spectra are shown in Fig. 2. In addition to the

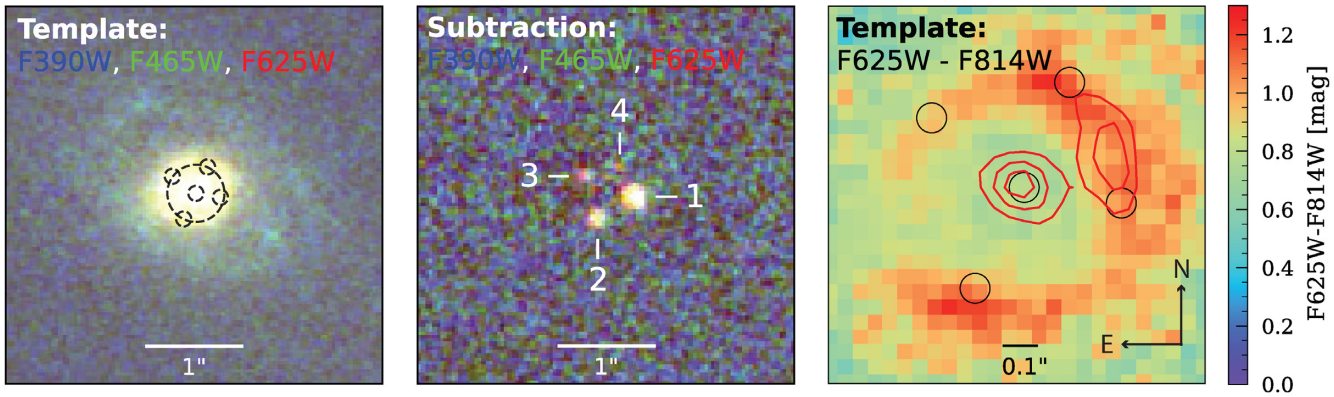

Figure 3. Left-hand panel: *HST* template images of the lens and host galaxies obtained after the SN faded. We note that the lens galaxy has a faint, diffuse blue halo. Middle panel: A difference image between the template and SN images (from 2016-10-25). Right-hand panel shows the $F625W - F814W$ colour of the lens and host galaxy system from template *HST* images (zoomed in on the central 1 arcsec × 1 arcsec). The red contour lines show the brightness distribution in $F814W$, indicating that the bright lens galaxy centre has an observed colour $F625W - F814W \approx 0.8$ mag, whereas the lensed host galaxy ring has a colour that varies between $F625W - F814W \approx 0.9$–1.3 mag.

Table 1. Log of spectroscopic observations of iPTF16geu used in this analysis.

UT date	MJD	Phase (d)	Telescope+Instrument	Slit width (arcsec)	Grism/grating	Resolution (λ/Δλ)	Source
2016-10-02.23	57663.23	+7.4	P60+SEDM	–	Lenslet array	100	Goobar et al. (2017)
2016-10-04.22	57665.22	+8.8	P200+DBSP	1.5	600/4000	740	Goobar et al. (2017)
2016-10-06.13	57667.13	+10.2	P200+DBSP	2.0	600/4000	560	Goobar et al. (2017)
2016-10-09.90	57670.90	+12.8	NOT+ALFOSC	1.0	Grism # 4	360	Goobar et al. (2017)
2016-10-15.87	57676.87	+17.1	GTC+OSIRIS	1.0	R1000R	670	Cano et al. (2018)
2016-10-18.00	57679.00	+18.6	VLT+XSHOOTER	1.0/0.9/0.9	UVB/VIS/NIR	5400/8900/5600	Cano et al. (2018)
2016-10-22.34	57681.34	+20.3	DCT+DeVeny	1.5	300	920	This work
2016-10-25.33	57686.33	+23.8	Keck+DEIMOS	1.2	600ZD	1100	This work
2016-10-26.19	57687.10	+24.3	P200+DBSP	1.5	600/4000	740	This work
2016-10-30.01	57691.01	+27.1	VLT+XSHOOTER	1.0/0.9/0.9	UVB/VIS/NIR	5400/8900/5600	Cano et al. (2018)
2016-11-02.24	57694.24	+29.4	Keck+LRIS	1.0	400/3400+400/8500	890	This work
2016-11-02.27	57694.27	+29.4	*HST*+WFC3/IR	–	GRISM256 G102	210	This work
2016-11-18.86	57710.86	+41.2	GTC+OSIRIS	1.0	R1000R	670	Cano et al. (2018)
2016-11-28.21	57720.21	+47.9	Keck+LRIS	1.0	400/3400+400/8500	890	This work
2016-11-30.82	57722.82	+49.7	GTC+OSIRIS	1.0	R1000R	670	Cano et al. (2018)
2016-12-15.81	57737.81	+60.3	GTC+OSIRIS	1.0	R1000R	670	Cano et al. (2018)
2019-05-24.46	58627.46	–	P200+DBSP	1.5	600/4000	740	This work
2019-06-26.46	58660.46	–	P200+DBSP	1.5	600/4000	740	This work

previously unpublished spectra presented here, we also analyse the early spectra from Goobar et al. (2017) and the GTC+OSIRIS and VLT+XSHOOTER spectra from Cano et al. (2018). All our spectra are available from the WISeREP archive[1] (Yaron & Gal-Yam 2012).

The long-slit spectra presented here were reduced in a standard fashion using `IRAF`[2] routines. To reduce and extract the P200+DBSP and Keck+LRIS spectra we use the custom `pyraf-dbsp` and `LPipe` pipelines (Bellm & Sesar 2016; Perley 2019). All ground-based spectra were observed using a slit width of ∼1–2 arcsec, covering all four SN images including the lens and host galaxies. The spectra were observed at parallactic angle, except the two VLT+XSHOOTER spectra, which were observed at $PA = +86$ deg.

We note that the GTC+OSIRIS spectra from Cano et al. (2018) have not been corrected for telluric lines and suffer from fringing and second-order contamination above 8300 Å.

The VLT+XSHOOTER spectra were observed using two AB nod-on-slit cycles, with an 'additional flexure compensation' observing block inserted in between. The ESO XSHOOTER pipeline is used for bias subtraction, flat-field correction, wavelength, and flux calibration using spectrophotometric standards, and sky-subtraction of the spectra taken at each position of the slit. We use pre- and post-processing scripts from Selsing et al. (2019)[3] to remove cosmics, extract, and combine the 1D spectra. Telluric lines are corrected using Molecfit and the parameter file provided by ESO.

We also obtained one epoch of slitless spectroscopy using *HST* WFC3/IR GRISM256/G102. We chose a grism orientation that would allow the traces from the brightest Images 1 and 2 to be extracted separately (at the cost of contaminating the spectrum of

[1] http://wiserep.weizmann.ac.il.

[2] The Image Reduction and Analysis Facility is distributed by the National Optical Astronomy Observatory, which is operated by the Association of Universities for Research in Astronomy (AURA) under cooperative agreement with the National Science Foundation (NSF).

[3] https://github.com/jselsing/xsh-postproc.

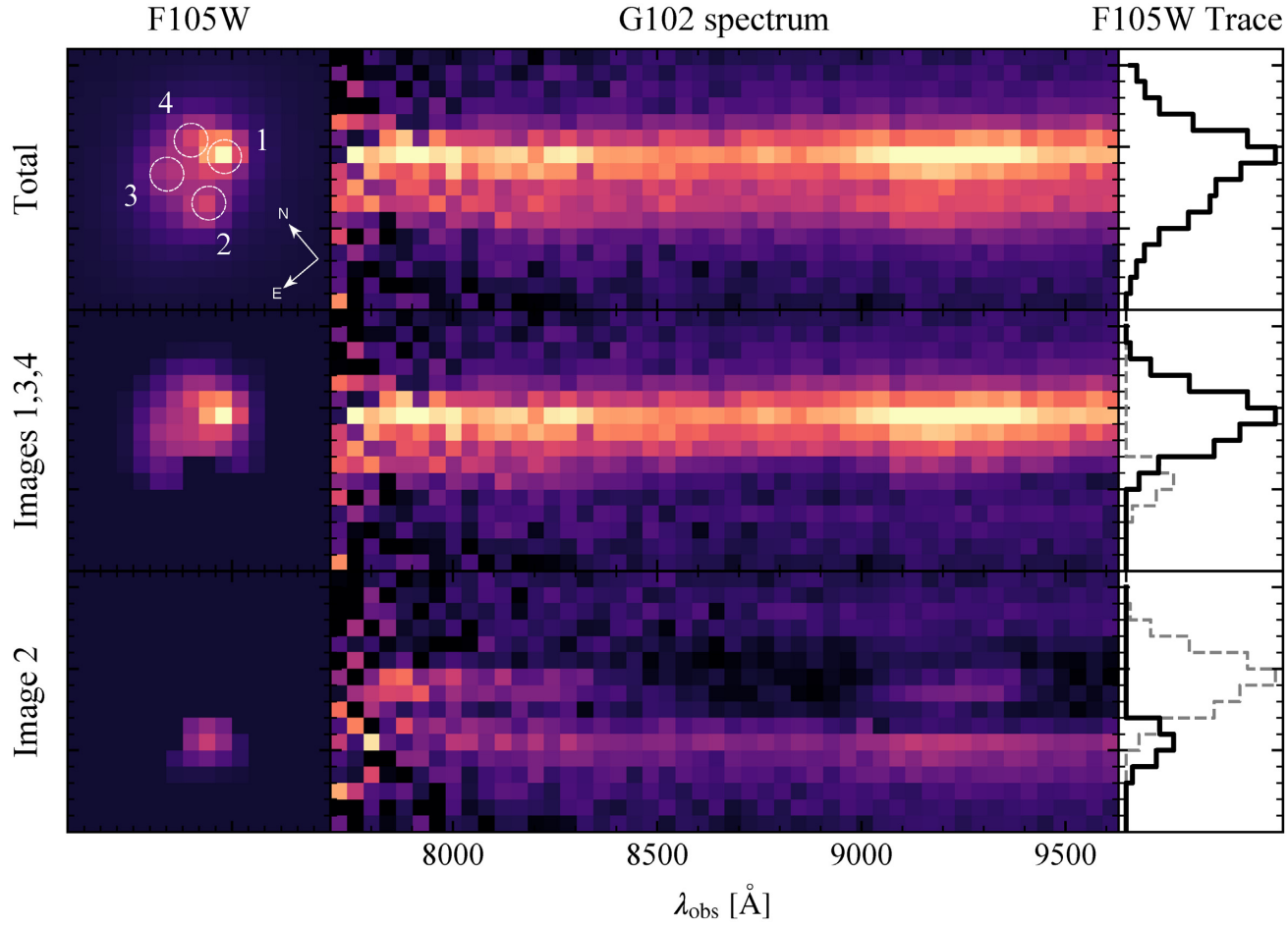

Figure 4. *HST F*105*W* direct imaging (left column), *HST G*102 grism spectra of the resolved lens images (centre), and collapsed *F*105*W* trace used for optimal 1D extraction (right) for the lens and host galaxies (top row). Grism spectra for Images 1, 3, and 4 (middle row) and Image 2 (bottom) are separately extracted. The 1D spectra of the image groupings are extracted from the contamination-subtracted grism spectra (centre) using the masked *F*105*W* trace (right) as the optimal extraction profile (solid black line; other trace shown as dashed grey line).

Image 1 with the fainter Images 3 and 4). The grism spectra were reduced using `GRIZLI` (see Brammer 2019; Wang et al. 2019),[4] a tool to reduce, model, and extract slitless spectra. `GRIZLI` first performs raw processing of direct *F*105*W* and G102 exposures, makes a composite *F*105*W* image, and constructs a source catalogue and segmentation map (with various individual internal steps performed with AstroDrizzle and SExtractor; Bertin & Arnouts 1996). Individual grism exposures are then corrected for contamination from the other sources using iterative contamination modelling, using the masked *F*105*W* image of each source as the spatial profile (e.g. as in Abramson et al. 2020).

Composite 2D grism spectra for each source are then constructed from these contamination-corrected individual exposures (see Fig. 4). Finally, we extract optimally weighted 1D spectra (Horne 1986) for each source from the composite 2D spectra, adopting the collapsed composite masked *F*105*W* image trace as the optimal spatial profile. In this analysis, the *F*105*W* image and G102 grism spectra are split into two parts, where we extract two separate spectra: the first corresponding to a blend of Images 1, 3, and 4 (Image 1 being the dominant), and a second being Image 2 (the second brightest, south-east image).

[4]Using v0.2.1-39, from https://github.com/gbrammer/grizli.

3 THE IPTF16GEU LENS AND HOST GALAXIES

Unlike the case of e.g. strongly lensed quasars, we are able to separately observe the lens and host galaxy system before and after the SN was active. Besides allowing us to study the lens and host galaxy properties, we can use pre- and post-SN data to remove the lens and host galaxy contribution from the observed SN spectra.

Two years after the SN explosion, we obtained a low signal-to-noise spectrum of the lens and host galaxy system combining two epochs of P200+DBSP observations with 900 and 1800 s exposure time, covering 3500–10 000 Å (black line in Fig. 5). To further disentangle the contributions from the lens and host galaxies to the total flux over a wider wavelength range, we construct a model spectral template of the combined lens and host galaxies. To do this, we use broad-band photometric data of the lens+host system from the SDSS (*ugriz* filters), Pan-Starrs (*grizy* filters), and 2MASS (*JHK* filters) surveys predating the SN, as well as our *HST* template images (*F*390*W*, *F*475*W*, *F*625*W*, *F*814*W*, *F*110*W*, and *F*160*W* filters, observed after the SN faded). We then use the models of the lens and host galaxy light in Dhawan et al. (2020) to compute the fractional fluxes of the lens and host galaxies (blue and red symbols in Fig. 5, respectively) within a 1 arcsec diameter aperture for all filters. We then fit for a combination of two galaxy template SEDs (Elliptical/S0/Sa/Sb or Sc) from Mannucci et al. (2001) at the

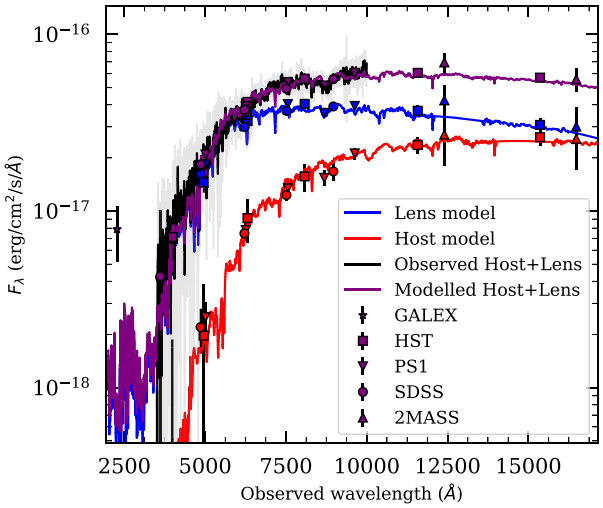

Figure 5. SED of lens and host galaxies. Purple symbols show broad-band *GALEX*, *SDSS* (*ugriz*), Pan-Starrs (*grizy*), 2MASS (*JH*), and *HST* photometry of the lens and host galaxies. The blue line is the lensing galaxy at $z = 0.2163$ (reddened by galactic extinction, $E(B-V)_{\rm MW} = 0.073$ mag), the red line is the host galaxy at $z = 0.4087$ [reddened by extinction in the MW and the lensing galaxy, $E(B-V)_{\rm lens} = 0.30$ mag]. The purple line is the sum of both galaxy template spectra. The black line is a P200+DBSP spectrum, observed in 2019 after the SN faded.

lens and host redshifts. Fig. 5 shows the best-fitting lens and host galaxy SED (blue and red lines in Fig. 5, respectively) and the total lens+host SED (purple symbols and line).

While we have little information on the morphology of the lens and host galaxy, we note that the fitted Sérsic indices of the central lens galaxy core (within 0.3 arcsec) from *HST* and Keck AO images range between 0.8 and 1.6, which is consistent with that of an Elliptical or a Bulge galaxy. As seen in Fig. 3, there is a faint extended blue halo (possibly spiral arms) around the bright lens galaxy core, and weak emission lines from Hα, [N II], and [O II] at the lens rest frame on top of broader absorption features. Similarly, weak emission lines from Hα, [N II], and [O II] are also seen at the host redshift.

Dhawan et al. (2020) used the SN images to measure the extinction along the line of sight towards the four point-like SN images, in both the lens and host galaxies. They found $E(B-V)_{\rm host} = 0.18$ mag for $R_V^{\rm host} = 2.0$, and $E(B-V)_{\rm lens} = 0.26$, 0.41, 0.78, and 1.58 mag with $R_V^{\rm lens} \sim 1.8$ for Images 1, 2, 3, and 4, respectively (all colour excesses are expressed at their respective rest frames). To verify the assumptions on the *average* dust extinction of the host galaxy by the lens in our spectra (observed through typical slit widths of $\sim$1 arcsec), we investigate the colour of the lensed host galaxy ring. Along the host galaxy ring, we measure $F625W - F814W = 0.9$–1.3 mag, while the brightest host galaxy spot (between Images 1 and 4) has a colour of $F625W - F814W \approx 1.1$ mag (see right-hand panel in Fig. 3). The observed $F625W - F814W$ colour of an unreddened Ellipctical (Sa) galaxy template at the host redshift is 0.89 (0.81) mag. This motivates us to redden the host galaxy SED by an average $E(B-V)_{\rm lens} \approx 0.3$ mag, i.e. close to the value derived from the light-curve fits $E(B-V)_{\rm lens} = 0.26$ mag for Image 1.

3.1 Redshift and velocity dispersion of the lens

In the SN and galaxy spectra we see narrow emission lines from the [O II] λ3727 doublet, Hα, [N II] (and weak emission from of [S II]) at the lens galaxy redshift, indicating a low level of star formation.

Goobar et al. (2017) analysed the emission lines visible in the early, low-resolution, SN spectra and measured the lens galaxy redshift ($z_{\rm lens} = 0.216$), and gave a first estimate of line-of-sight velocity dispersion, $\sigma_v = 163^{+41}_{-27}$ km s^{-1}, of the lensing galaxy from the combined widths of the Hα and [N II] lines.

Here, we use our highest resolution spectra (the two VLT+XSHOOTER spectra) and fit Gaussian profiles to the emission lines. We do this after normalizing the spectra, fitting low-order polynomials to the continuum level around the regions of interest. The most prominent emission lines are shown in Fig. 6 for the lens galaxy (top panels) and host galaxy (bottom panels). From these lines we determine the redshift of the lens, $z_{\rm lens} = 0.2163 \pm 0.0001$.

In the VLT+XSHOOTER spectra, we note that the lens galaxy Hα emission line is affected by Balmer absorption from stellar atmospheres (seen from extrapolating the stellar continuum fit, shown as a blue dashed line in the upper right panel of Fig. 6) and hence the true strength is underestimated.

For the lensing galaxy, we measure the equivalent widths (EW) of the Ca II H&K and Na ID absorption features to be 11.5 and 2.3 Å, respectively. Both features are centred at the lens rest-frame redshift (see Figs 6 and 7).

In order to estimate the velocity dispersion of the lens galaxy, we perform stellar continuum fitting with pPXF (Cappellari & Emsellem 2004; Cappellari 2017). pPXF models a galaxy spectrum G as a convolution between template spectra T and the line-of-sight velocity distribution (LOSVD) of the stars $\mathcal{L}$

$$G_{\rm mod}(x) = T(x) * \mathcal{L}(cx),$$

where $x = \ln \lambda$.

In the late-time SN spectra, as well as the post-SN spectra, the flux below $\sim$5500 Å is dominated by the lens galaxy. For the VLT+XSHOOTER ($R \approx 5400$) spectra, we use the high resolution PEGASE models (Le Borgne et al. 2004), spanning the wavelength range 3900–6800 Å at an FWHM $\sim$0.55 Å and having ages and metallicities in the range $t = 1$–2×10^4 Myr and $Z = 0.0004$–0.1. We mask the [O II] line from the host, and use the lens rest-frame wavelength range 3900–4550 Å (to avoid Ca II H&K from the host) in the XSHOOTER spectrum, giving a best-fitting velocity dispersion $\sigma = 129 \pm 4$ km s^{-1}. The data and fit are shown in Fig. 7. This measured velocity dispersion is lower than the previous estimate (Goobar et al. 2017), and matches the expected velocity dispersion $\sigma_{\rm mod} = 132^{+4}_{-7}$ km s^{-1} from the lens modelling in Mörtsell et al. (2020).

As a consistency check, we also fit our low-resolution ($R \sim 1000$) Keck+LRIS, Keck+DEIMOS and post-SN P200+DBSP spectra using the UV-extended MILES templates (eMILES; Vazdekis et al. 2016). These single-age, single-metallicity stellar population spectra and have a resolution of 2.51 Å (FWHM) in the range 3540–8950 Å. These spectra yield similar best-fitting values of the velocity dispersion, but with larger errorbars ($\sim$25 km s^{-1}).

3.2 The host galaxy of iPTF16geu

Thanks to the high lensing magnification we are able to study the structure and time evolution of interstellar absorption lines for SNe Ia at cosmological distances, at a level previously only possible a small subset of very nearby SNe Ia (e.g. Goobar et al. 2014; Ferretti et al. 2016, 2017).

Similar to the lens galaxy, we also detect narrow emission lines from [O II] λ3727, Hα, [N II] at the host galaxy redshift. From these lines we determine the and host galaxy redshift, $z_{\rm host} = 0.4087 \pm 0.0001$ (see bottom right panel of Fig. 6).

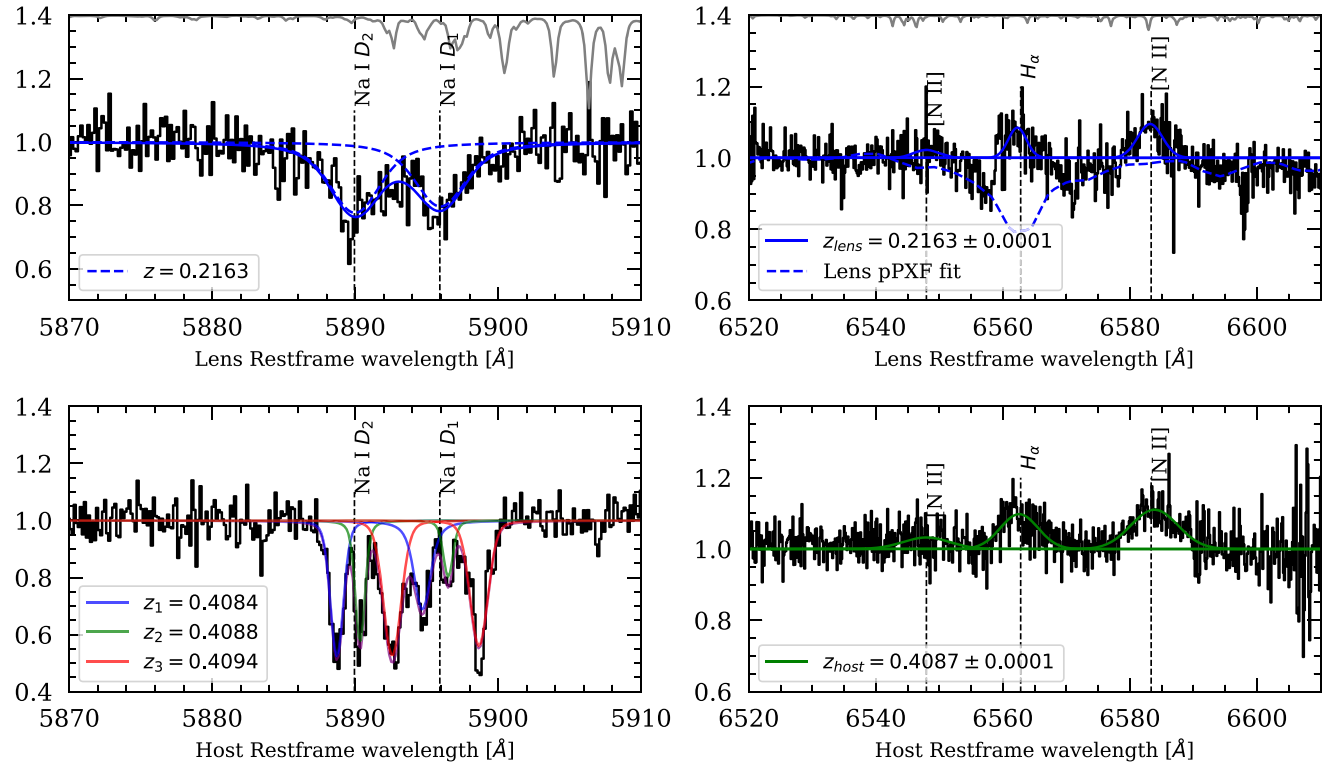

Figure 6. Zoomed in panels on narrow Na ID absorption lines, Hα and [N II] emission lines at the lens ($z_{\rm lens} = 0.2163$) and host ($z_{\rm host} = 0.4087$) rest frames (marked by vertical black dashed lines in the panels) in the VLT+XSHOOTER spectrum from 2016 October 30 (+27 d after maximum light). The grey line at the top of the upper panels shows the telluric lines, which have been removed from the spectra.

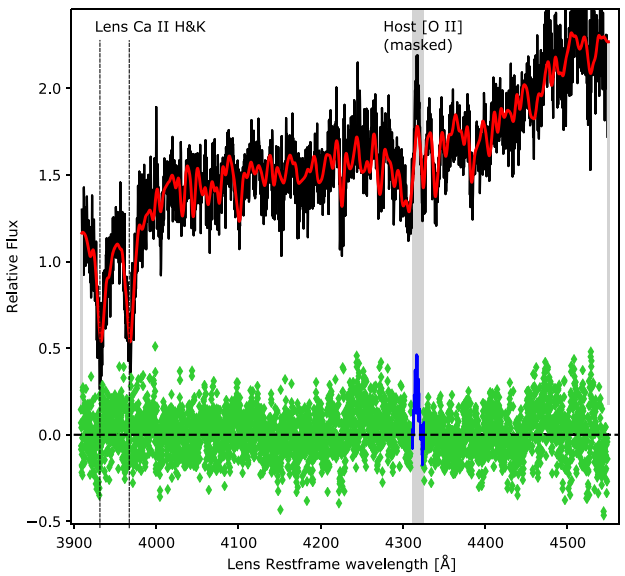

Figure 7. pPXF fit of the lens galaxy. The black line is part of the UVB-arm XSHOOTER spectrum from 2016 October 30, red line is the best fit PEGASE template and green symbols show the residuals. The dashed lines indicate the lens galaxy Ca II H & K absorption lines and the grey shaded area shows the masked-out [O II] line from the host galaxy.

For Na I D, we resolve three distinct, narrow components (FWHM ∼44–79 km s^{-1}, see bottom left panel of Fig. 6) at $v_1 = -61$, $v_2 = 23$, and $v_3 = 139$ km s^{-1}, with respect to the galaxy rest frame (defined by the emission lines). For the first XSHOOTER epoch at +18.6 d we measure a total Na ID $EW = 3.9$ Å, and for the second epoch $EW = 3.3$ Å at +27.1 d. The EWs are listed in Table 2.

The equivalent width of the Na ID lines is a commonly used proxy for dust reddening, $E(B-V)$ (see e.g. Munari & Zwitter 1997; Poznanski et al. 2011; Poznanski, Prochaska & Bloom 2012; Phillips et al. 2013). It should be noted that these relations are typically well-defined for $EW < 1.0$ Å and that the theoretical relation is between EW and optical depth, $\tau \sim A_V$, rather than the colour excess $E(B-V)$. None the less, applying commonly used relations (Barbon et al. 1990; Turatto, Benetti & Cappellaro 2003; Poznanski et al. 2011) with $EW^{\rm Na\,id}_{\rm host} = 3.9$ Å yields a wide range of $E(B-V)_{\rm host} \sim 0.6$–$1.9$ mag, with little predictive power.

The light-curve fits (Dhawan et al. 2020) indicate that the host extinction is $E(B-V)_{\rm host} = 0.18$–0.29 mag (depending whether the total-to-selective absorption ratio is fixed to $R_V = 2.0$, 3.1 or treated as a free parameter). iPTF16geu therefore seems to be another case of an SN Ia displaying 'anomalously' strong Na ID absorption (Phillips et al. 2013).

We do not detect any absorption lines from Diffuse Interstellar Bands (e.g. DIB λ5780, which has been suggested to be an even better proxy for dust extinction).

4 SUPERNOVA FEATURES AND THEIR TIME-EVOLUTION

Cano et al. (2018) found that iPTF16geu can be classified as a high-velocity ($v^{\rm max}_{\rm Si\,II\lambda6355} = 11950 \pm 140$ km s^{-1}), high-velocity gradient ($\dot{v} = -110.3 \pm 10.0$ km s^{-1}) and 'core-normal' SN Ia. The strength of various features (measured though their pseudo-equivalent widths) argue against SN iPTF16geu being a faint, broad-lined, cool, or

Table 2. Measured pseudo-equivalent widths (pEW) and Si II λ6355 line velocities for iPTF16geu. Last two columns list the total Na ID equivalent widths for the lens and host galaxies from our highest resolution spectra.

Phase (d)	pEW1 (Å)	pEW3 (Å)	pEW4 (Å)	pEW7 (Å)	pEW8 (Å)	$v_{\rm Si\,II\lambda6355}$ (10^3 km s^{-1})	Lens Na ID EW (Å)	Host Na ID EW (Å)
7.4	103 (19)		157 (35)	92 (34)				
8.8	101 (18)	167 (35)	192 (35)	117 (32)		11.66 (0.47)		
10.2	70 (9)	177 (25)	212 (23)	153 (20)		11.38 (0.53)		
12.8	89 (13)	286 (32)	290 (33)	102 (18)		11.22 (0.97)		
17.1	85 (9)	313 (13)	327 (14)	129 (10)		10.92 (0.12)		
18.6	64 (14)	277 (31)	291 (30)	224 (31)	451 (38)	10.85 (0.36)	2.4 (0.1)	3.9 (0.1)
20.3		296 (27)	374 (34)					
23.8	108 (16)	283 (28)	368 (36)	186 (24)		10.57 (0.19)	2.3 (0.2)	3.5 (0.2)
24.3		281 (42)	358 (58)	261 (39)		10.65 (0.29)		
27.1	137 (26)	212 (37)	352 (57)	277 (42)	487 (63)	10.66 (0.15)	2.3 (0.1)	3.3 (0.1)
29.4	164 (18)	200 (25)	370 (40)	241 (32)		10.59 (0.21)		
47.9	129 (37)	131 (57)	273 (93)	230 (73)				
49.7	13 (28)	226 (92)	391 (127)					

shallow-silicon SN Ia (note however that no maximum light spectrum is available, which is typically used for making these classifications).

Using more data, and a refined lens and host galaxy template spectrum, we will measure the pseudo-equivalent widths (pEWs) and Si II line expansion velocities. As demonstrated in Cano et al. (2018), accurate removal of the lens- and host galaxy contribution is crucial in order to measure the intrinsic SN pEWs. For this purpose, we can choose to subtract our observed or model lens+host galaxy spectrum from the SN observations. While they yield similar results, the model spectrum allows us to measure pEW1 and pEW8, due to the wider wavelength range. We first subtract the lens and host galaxy contamination from the observed spectra, scaling the observed spectra with a constant factor, so that the subtracted spectra match the template subtracted photometry (this scaling typically varies between 0.8 and 1.2, accounting for imperfect absolute flux calibration, varying degrees of host galaxy removal in the different reduction procedures, etc.). While the spectra could in practice also suffer from wavelength-dependent calibration offsets (due to slit-losses, atmospheric dispersion etc.), we do not attempt to correct for this, since this might erase any chromatic micro-lensing signatures. Synthetic photometry of the subtracted SN spectra shows good agreement with the subtracted photometry, typically within ∼10 per cent precision. Furthermore, we de-redden the summed spectra with the best-fitting lens and host galaxy extinction parameters found by Dhawan et al. (2020), using $E(B-V)^{\rm host} = 0.18$ mag with $R_V^{\rm host} = 2.0$, $E(B-V)^{\rm lens,\,1} = 0.26$ mag with $R_V^{\rm lens,1} = 1.8$ (since the ground-based spectra are dominated by the light from Image 1) and $E(B-V)_{MW} = 0.073$ mag.

To compute the pseudo-equivalent widths (pEWs) and Si II line expansion velocities, we use the SPEXTRACTOR code (Papadogiannakis et al., in preparation).[5] Instead of fitting a series of Gaussians to the absorption features, SPEXTRACTOR measure the pEWs and absorption minima through model-independent Gaussian processes.

In our spectra, ranging between +7 to +60 days from peak brightness, we can measure pEW1 (Ca II H&K), pEW3 (Mg II), pEW4 (Fe II), pEW7 (Si II 6355), and pEW8 (Ca II IR) (following the conventions in Folatelli 2004; Garavini et al. 2007; Folatelli et al. 2013). Fig. 8 shows an example of a lens and host galaxy subtracted, de-reddened VLT+XSHOOTER spectrum from 2016 October 18.

[5]Code is publicly available at github.com/astrobarn/spextractor.

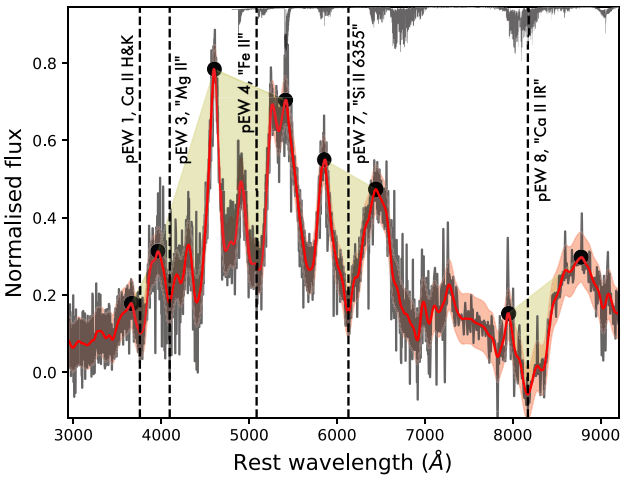

Figure 8. Example of pseudo-Equivalent Width measurements using SPEXTRACTOR. The black line is a lens and host subtracted VLT+XSHOOTER spectrum from 18.6 d after maximum light, the red line is the Gaussian process smoothed spectrum, the yellow regions show the measured pEWs, and the black dashed lines indicate the fitted absorption line minima. The grey line at the top of the panel shows the telluric lines, which have been removed from the spectrum.

It includes the smoothed spectrum (red line), the pEW features and absorption line minima fitted by SPEXTRACTOR.

We measure the Si II λ6355 line expansion velocities for all our spectra. Using data between +7 and +20 d after maximum (although the clear identification with Si II λ6355 is only valid until day ∼+10), we find a linear slope of the Si II expansion velocity, $\dot{v} = -82 \pm 13$ km s^{-1} d^{-1}, which is slower than what Cano et al. (2018) report for the same data ($\dot{v} = -110 \pm 10$ km s^{-1} d^{-1}, see Fig. 9). Hence, the velocity gradient for iPTF16geu is more comparable to the normal sub-class in Folatelli et al. (2013) ($\dot{v} = -86 \pm 14$ km s^{-1} d^{-1}), rather than the high-velocity gradient subclass. However, from the linear fit we extrapolate the velocity at $t_{B,\,\rm max}$ to be $v_{B,\,\rm max} = 12100 \pm 220$ km s^{-1}, which would make iPTF16geu a high-velocity SN Ia (following the definitions in Wang et al. 2009; Folatelli et al. 2013). We note that our velocities are systematically higher (by ∼400 km s^{-1}) than in Cano et al. (2018).

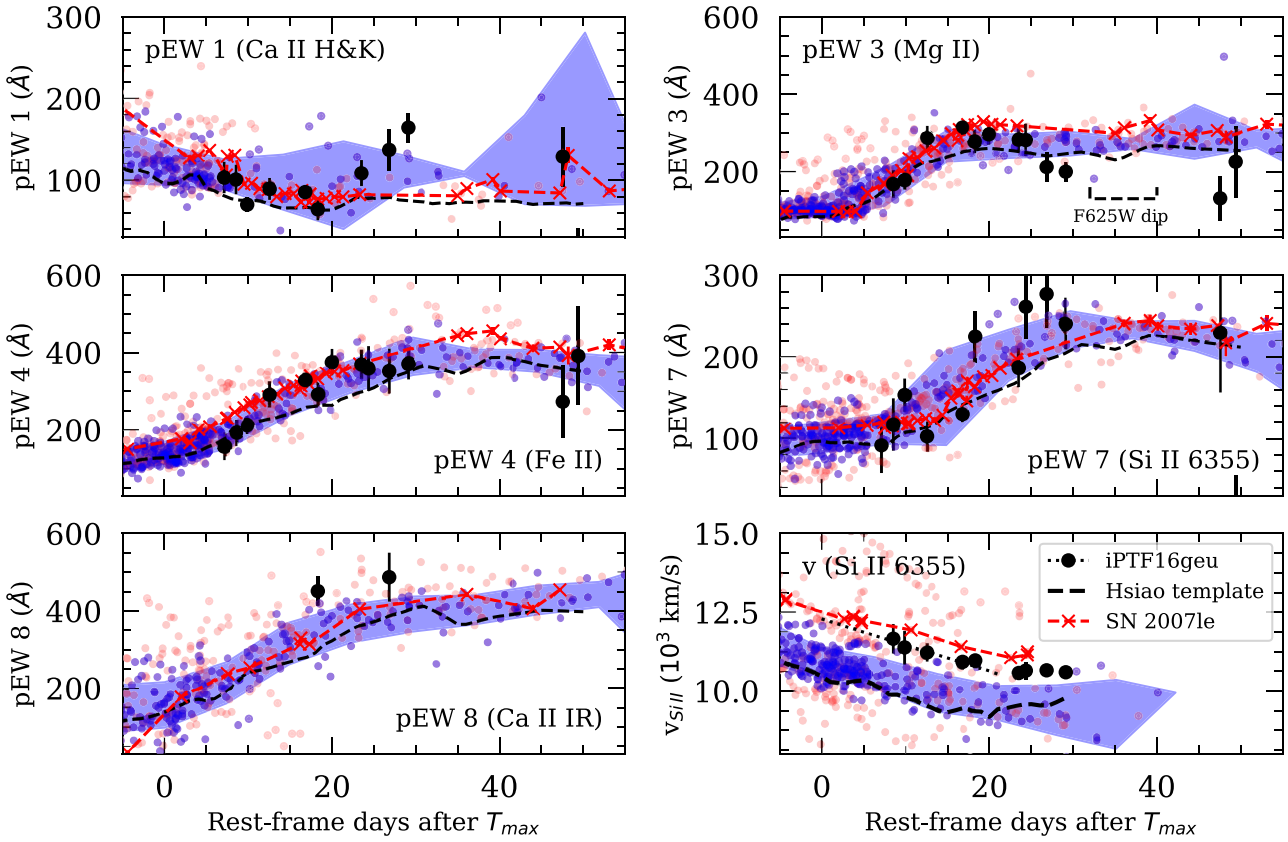

Figure 9. Time evolution of the pEWs for features 1, 3, 4, 7, and 8 together with the Si II expansion velocity evolution (bottom right panel). Black circles are the measured pEWs after lens- and host galaxy subtraction and de-reddening. Transparent points and shaded bands are individual measurements and the binned mean ($\pm 1\sigma$) of low-redshift SNe from Folatelli et al. (2013), for all (red) and 'Normal' (blue) SNe Ia in their sample. The black and red dashed lines shows the pEW and velocity evolution of the Hsiao template and SN 2007le, respectively.

Turning to the pEW measurements, we do not see any significant deviations from the time-evolution of SNe Ia in Folatelli et al. (2013). In Fig. 9, the black points show the pEW measurements of iPTF16geu compared to all (red points) or 'normal' (blue points and blue shaded region) SNe Ia in Folatelli et al. (2013). However, we note that some measurements are outside the 1σ range, e.g. late-time pEW1 (likely due to improper lens and host galaxy removal), pEW3 and pEW7 (where the telluric corrections are imperfect).

5 TIME-DELAY MEASUREMENTS FROM SPECTRA OF SPATIALLY RESOLVED LENS IMAGES

In our single epoch of *HST* spectroscopy, we can spatially resolve two spectra: one spectrum corresponding to Image 2 and one spectrum corresponding to Images 1, 3, and 4. However, Images 3 and 4 are subdominant, contributing with 7 per cent and 5 per cent to the total flux in *F*814*W* at this epoch, respectively. Hence, we will treat this spectrum as stemming from Image 1. By comparing the time evolution of spectral features between the spectra, we can in principle provide an independent measurement of the time delays between the SN images. However, in our case we are limited by the coarse ($R \sim 210$) spectral resolution. To complicate things further, at the epoch (+29 d) the Si II absorption feature is no longer well-defined, displaying two or more local minima.

Age dating of SN spectra is routinely done using cross-correlation techniques (e.g. SNID; Blondin & Tonry 2007), and have been successful in measuring cosmic time-dilation (Blondin et al. 2008). We construct a simple χ^2-statistic, fitting Hsiao template spectra (Hsiao et al. 2007) at different phases to the spectra of the spatially resolved SN images. This allows us to simultaneously fit for residual lens and host galaxy contamination using our template spectrum, and subtract a fraction of that flux (0.80 ± 0.03 and 0.19 ± 0.02 for Images 1 and 2, respectively) from the resolved SN spectra, so that the subtracted SN spectra and Hsiao templates at each phase match the host subtracted *F*814*W* photometry (see upper panel of Fig. 10).

The best-fitting phases for the Hsiao templates are $+30.0^{+2.5}_{-2.2}$ d for Image 1 and $+31.0^{+3.8}_{-3.5}$ d for Image 2. Assuming an SN stretch, $s = 1.0$, this corresponds to $T_{\rm max,\,1} = 57652.0$ and $T_{\rm max,\,2} = 57650.6$, which corresponds to an observed time-delay between images 1 and 2 of $\Delta t_{12} = -1.4^{+4.6}_{-4.1}$ d.

This is, to our knowledge, the first spectroscopic time-delay ever measured. The time delay is compatible, but less constraining, than the time-delay measurements from light-curve fits in Dhawan et al. (2020), where they find $T_{\rm max,\,1} = 57652.80(\pm 0.33)$ and $T_{\rm max,\,2} = 57652.57(\pm 0.99)$, which corresponds to an observed time-delay between images 1 and 2 of $\Delta t_{12} = -0.23 \pm 1.04$ d. These findings are also in agreement with the expected time-delay $\Delta t_{12} = -0.1$ to -0.6 d from the lens models in More et al. (2017) and Mörtsell et al. (2020).

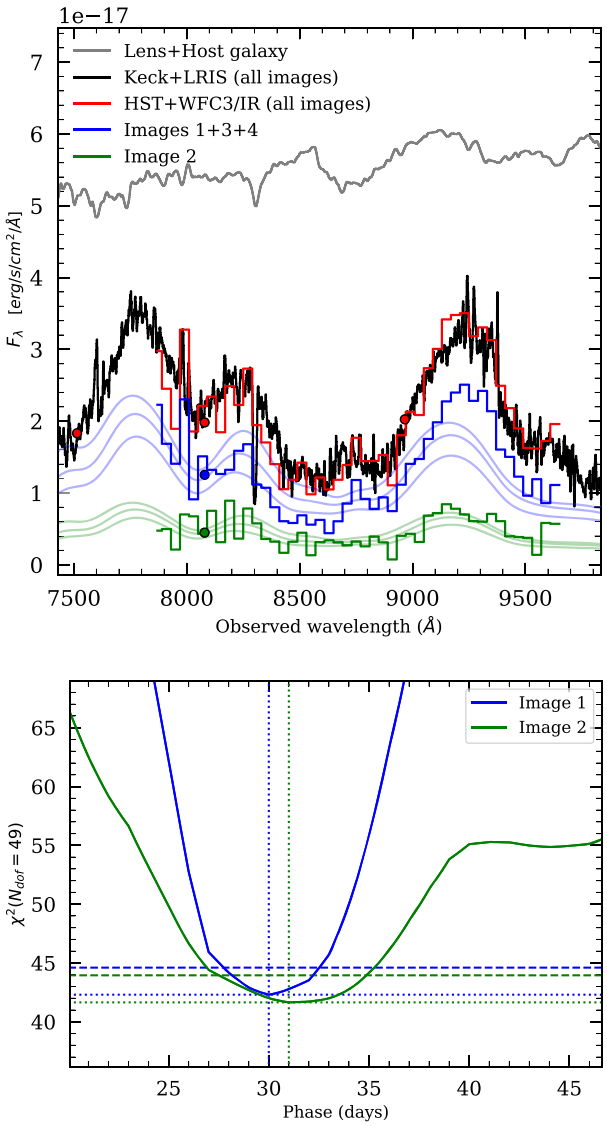

Figure 10. Top panel: *HST* spectra of the spatially resolved Images 1 + 3 + 4 (blue line) and Image 2 (green line). The summed spectra (red line) show very good agreement with the ground-based Keck spectrum (black line), observed at the same time. Bottom panel: χ^2 minima of the fitted phases for Images 1 (blue line) and Image 2 (green line).

The fits are weakly dependent on the choice of lens and host galaxy template (i.e. if we use the modelled or observed spectrum), and insensitive to fitting reddened or unreddened Hsiao template SEDs. We also tried using the SED template of SN 2011fe (Amanullah et al. 2015), which gives best-fitting phases $31.1^{+2.9}_{-3.3}$ and $32.8^{+2.9}_{-5.7}$ d for Images 1 and 2, corresponding to an observed time-delay, $\Delta t_{12} = -2.4^{+4.0}_{-8.9}$ d).

6 DISCUSSION

Much attention has recently been given to microlensing effects, especially how chromatic distortion of the supernova spectra affect light-curve and time-delay measurements (Suyu et al. 2020). While the light-curve analysis and lens modelling indicate that Image 1 (and possibly Image 2) is additionally magnified by microlensing, we do not see any obvious spectroscopic signs of chromatic microlensing effects.

We do note a small dip in the *F*625*W* light curve of Image 1 ($\Delta m \sim 0.3$ mag, also seen in the summed photometry in Fig. 1) around 50 d after peak brightness. This dip is only seen for Image 1 in two *F*625*W* epochs (2016 November 10 and November 15), and is not seen for the other images nor in the other *HST* filters. Unfortunately, there are no spectroscopic observations during this dip. However, we do see a small decrease in pEW3 (covered by *F*625*W*) just before the onset of the dip.

While the pEW evolution could be a useful tool to detect or constrain chromatic lensing effects, it is difficult to quantify (both observationally and from simulations). For example, the pEWs are at all times consistent with the binned mean of the *sample* of normal SNe Ia in Folatelli et al. (2013), while if we compare the pEW evolution to an *individual* SN, the deviations as a function of wavelength and time can be larger or smaller depending on which SN we choose. Using SNID (Blondin & Tonry 2007) to cross-correlate the iPTF16geu spectra with a library of well studied SNe Ia, SN 2007le (Simon et al. 2009) appears among the top matches. In Fig. 9, we show the pEWs and Si II expansion velocity as function of time for iPTF16geu (black symbols) which closely follows the values for SN 2007le (crosses and red dashed lines). With the current precision of our meaurements, we do not see any significant deviations of the pEWs ($>3\sigma$) with respect to the SN Ia sample or SN 2007le.

Turning to the strong Na ID absorption features in the host galaxy of iPTF16geu, it is interesting to note that the deepest absorption feature is the most redshifted, placing iPTF16geu in the 'blueshifted subclass' as defined in Sternberg et al. (2011). Phillips et al. (2013) studied a large sample of SNe Ia with high-resolution spectra, and found that all events with anomalously large Na ID column densities (in comparison to the derived dust extinction from their colors) belonged to this 'blueshifted subclass'. We also see a significant *decrease* of the total Na ID EW in our highest resolution spectra: the Na ID EW goes from 3.9 to 3.3 Å between VLT+XSHOOTER epochs at +18 and +27 d ($EW = 3.5$ Å in the Keck+DEIMOS spectrum at +24 d).

These facts also make a strong link to SN 2007le (Simon et al. 2009) which also showed strong, blueshifted, and time-variable Na ID absorption ($EW \sim 1.6$ Å) but was not highly reddened ($E(B-V) = 0.27$ mag).

It has been speculated that these SNe Ia, with strong, blueshifted absorption may belong to a distinct sub-population of SNe: having systematically higher ejecta velocities and redder colors at maximum brightness, preferentially residing in late-type galaxies (Foley et al. 2012; Maguire et al. 2013). High-resolution spectroscopy of gravitationally lensed SNe thus offer us a way to study the progenitor systems and the explosion properties of high-redshift SNe Ia.

7 SUMMARY AND OUTLOOK

In this paper, we have analysed the spectra of the lensed SN Ia iPTF16geu. Using high dispersion spectra, we fit the lens galaxy line-of-sight velocity dispersion, $\sigma = 129 \pm 4$ km s^{-1} at a redshift $z_{\rm lens} = 0.2163$. This value is lower than the previous estimate and compatible with the lens model in Mörtsell et al. (2020). Knowing the velocity dispersion of the lens breaks degeneracies in the lens modelling, e.g. between the slope of the lens mass distribution and H_0 (Jee et al. 2019; Mörtsell et al. 2020).

Using high angular resolution slitless spectroscopy, we derive a spectroscopic time delay between the two brightest images (Image 1 and 2).

In the future, resolving individual images of lensed supernovae (discovered early by e.g. ZTF and LSST) with Integral Field Spectrographs (e.g. MUSE with Adaptive Optics on the ESO Very Large Telescope or NIRSpec on the James Webb Space Telescope), could yield independent time-delay measurements with precision comparable to light-curve fits. Near maximum light, SNe Ia typically have expansion velocity gradients $\sim$100–250 km s^{-1} d^{-1}. Provided spatially resolved spectra of the SN images, the time delays can be measured to roughly one day precision (given that e.g. the expansion velocities of absorption lines of the SN is observed at early phases, when the expansion velocity gradient is higher). Since the typical expansion velocity decreases as $v_{\rm exp}(t) \propto t^{-0.22}$ (Piro & Nakar 2014), spectra at even earlier phases would allow time-delays measurements with precision better than one day.

ACKNOWLEDGEMENTS

We thank E. Zackrisson and A. Adamo for helpful discussions. We thank T. Brink, R. Bruch, Cooper, S. Goldwasser, A. Ho, I. Irani, B. Jain, Y. Sharma, A. Tzanidakis, Q. Ye, and W. Zheng for performing observations.

AG acknowledges support from the Swedish National Space Agency and the Swedish Research Council. RL is supported by a Marie Skłodowska-Curie Individual Fellowship within the Horizon 2020 European Union (EU) Framework Programme for Research and Innovation (H2020-MSCA-IF-2017-794467). ASC acknowledges support from the G.R.E.A.T research environment, funded by Vetenskapsrådet, the Swedish Research Council.

The Intermediate Palomar Transient Factory project is a scientific collaboration among the California Institute of Technology, Los Alamos National Laboratory, the University of Wisconsin, Milwaukee (USA), the Oskar Klein Center at Stockholm University (Sweden), the Weizmann Institute of Science, the TANGO Program of the University System of Taiwan, and the Kavli Institute for the Physics and Mathematics of the Universe.

Some of the data presented herein were obtained at the W.M. Keck Observatory, which is operated as a scientific partnership among the California Institute of Technology, the University of California, and the National Aeronautics and Space Administration. The Observatory was made possible by the generous financial support of the W.M. Keck Foundation. The authors wish to recognize and acknowledge the very significant cultural role and reverence that the summit of Mauna Kea has always had within the indigenous Hawaiian community. We are most fortunate to have the opportunity to conduct observations from this mountain.

These results made use of the Lowell Discovery Telescope at Lowell Observatory. Lowell is a private, non-profit institution dedicated to astrophysical research and public appreciation of astronomy and operates the DCT in partnership with Boston University, the University of Maryland, the University of Toledo, Northern Arizona University and Yale University. The upgrade of the DeVeny optical spectrograph has been funded by a generous grant from John and Ginger Giovale and by a grant from the Mt. Cuba Astronomical Foundation.

DATA AVAILABILITY

All our spectra are available from the WISeREP archive (Yaron & Gal-Yam 2012).

REFERENCES

Abramson L. E., Brammer G. B., Schmidt K. B., Treu T., Morishita T., Wang X., Vulcani B., Henry A., 2020, MNRAS, 493, 952
Amanullah R. et al., 2015, MNRAS, 453, 3300
Barbon R., Benetti S., Cappellaro E., Rosino L., Turatto M., 1990, A&A, 237, 79
Bellm E. C., Sesar B., 2016, Astrophysics Source Code Library, record ascl:1602.002
Bertin E., Arnouts S., 1996, A&AS, 117, 393
Blondin S., Tonry J. L., 2007, ApJ, 666, 1024
Blondin S. et al., 2008, ApJ, 682, 724
Brammer G., 2019, Astrophysics Source Code Library, record ascl:1905.001
Cano Z., Selsing J., Hjorth J., de Ugarte Postigo A., Christensen L., Gall C., Kann D. A., 2018, MNRAS, 473, 4257
Cappellari M., 2017, MNRAS, 466, 798
Cappellari M., Emsellem E., 2004, PASP, 116, 138
Dhawan S. et al., 2020, MNRAS, 491, 2639
Dobler G., Keeton C. R., 2006, ApJ, 653, 1391
Ferretti R. et al., 2016, A&A, 592, A40
Ferretti R., Amanullah R., Bulla M., Goobar A., Johansson J., Lundqvist P., 2017, ApJ, 851, L43
Folatelli G., 2004, New Astron. Rev., 48, 623
Folatelli G. et al., 2013, ApJ, 773, 53
Foley R. J. et al., 2012, ApJ, 752, 101
Foxley-Marrable M., Collett T. E., Vernardos G., Goldstein D. A., Bacon D., 2018, MNRAS, 478, 5081
Garavini G. et al., 2007, A&A, 470, 411
Goldstein D. A., Nugent P. E., 2017, ApJ, 834, L5
Goldstein D. A., Nugent P. E., Kasen D. N., Collett T. E., 2018, ApJ, 855, 22
Goldstein D. A., Nugent P. E., Goobar A., 2019, ApJS, 243, 6
Goobar A., Mörtsell E., Amanullah R., Nugent P., 2002, A&A, 393, 25
Goobar A. et al., 2014, ApJ, 784, L12
Goobar A. et al., 2017, Science, 356, 291
Horne K., 1986, PASP, 98, 609
Hsiao E. Y., Conley A., Howell D. A., Sullivan M., Pritchet C. J., Carlberg R. G., Nugent P. E., Phillips M. M., 2007, ApJ, 663, 1187
Huber S. et al., 2019, A&A, 631, A161
Jee I., Suyu S. H., Komatsu E., Fassnacht C. D., Hilbert S., Koopmans L. V. E., 2019, Science, 365, 1134
Le Borgne D., Rocca-Volmerange B., Prugniel P., Lançon A., Fioc M., Soubiran C., 2004, A&A, 425, 881
Maguire K. et al., 2013, MNRAS, 436, 222
Mannucci F., Basile F., Poggianti B. M., Cimatti A., Daddi E., Pozzetti L., Vanzi L., 2001, MNRAS, 326, 745
More A., Suyu S. H., Oguri M., More S., Lee C.-H., 2017, ApJ, 835, L25
Mörtsell E., Johansson J., Dhawan S., Goobar A., Amanullah R., Goldstein D. A., 2020, MNRAS, 496, 3270
Munari U., Zwitter T., 1997, A&A, 318, 269
Oguri M., 2019, Rep. Prog. Phys., 82, 126901
Oguri M., Marshall P. J., 2010, MNRAS, 405, 2579
Perley D., 2019, PASP, 131, 084503
Petrushevska T., Amanullah R., Bulla M., Kromer M., Ferretti R., Goobar A., Papadogiannakis S., 2017, A&A, 603, A136
Phillips M. M. et al., 2013, ApJ, 779, 38
Pierel J. D. R., Rodney S., 2019, ApJ, 876, 107
Piro A. L., Nakar E., 2014, ApJ, 784, 85
Poznanski D., Ganeshalingam M., Silverman J. M., Filippenko A. V., 2011, MNRAS, 415, L81
Poznanski D., Prochaska J. X., Bloom J. S., 2012, MNRAS, 426, 1465
Refsdal S., 1964, MNRAS, 128, 307
Selsing J. et al., 2019, A&A, 623, A92
Simon J. D. et al., 2009, ApJ, 702, 1157
Sternberg A. et al., 2011, Science, 333, 856

Suyu S. H. et al., 2020, A&A, 644, A162
Turatto M., Benetti S., Cappellaro E., 2003, in Hillebrandt W., Leibundgut B., eds, From Twilight to Highlight: The Physics of Supernovae, Springer, New York. p. 200
Vazdekis A., Koleva M., Ricciardelli E., Röck B., Falcón-Barroso J., 2016, MNRAS, 463, 3409
Wang X. et al., 2009, ApJ, 699, L139
Wang X. et al., 2019, ApJ, 882, 94
Yahalomi D. A., Schechter P. L., Wambsganss J., 2017, preprint (arXiv:1711.07919)
Yaron O., Gal-Yam A., 2012, PASP, 124, 668

This paper has been typeset from a TEX/LATEX file prepared by the author.